Upper limit of proton anisotropy and its relation to EMIC waves in the inner magnetosphere

Sung-Jun Noh[1], Dae-Young Lee[2], Hyomin Kim[1], Louis J. Lanzerotti[1], Andrew Gerrard[1], and Ruth M. Skoug[3]

[1]Center for Solar-Terrestrial Research,
New Jersey Institute of Technology,
Newark, New Jersey, USA
sjnoh@njit.edu

[2]Department of Astronomy and Space Science
Chungbuk National University,
Cheongju, Chungbuk 362-763, Korea

[3]Los Alamos National Laboratory, Los Alamos, New Mexico, USA

Key Points:

- Proton anisotropy has a clear upper bound that follows an inverse relationship with the plasma beta within a certain range.
- EMIC waves occur with an anisotropy below but close to the upper bound within a narrower plasma beta range.
- The anisotropy associated with EMIC waves is unstable to the linear instability, requiring a nonlinear process to set the upper bound.

Abstract

Proton anisotropy in velocity space has been generally accepted as a major parameter for exciting electromagnetic ion cyclotron (EMIC) waves. In this study, we estimate the proton anisotropy parameter as defined by the linear resonance theory using data from the Van Allen Probes mission. Our investigation uses the measurements of the inner magnetosphere ($L < 6$) from January 2013 to February 2018. We find that the proton anisotropy is always clearly limited by an upper bound and it well follows an inverse relationship with the parallel proton β (the ratio of the plasma pressure to the magnetic pressure) within a certain range. This upper bound exists over wide spatial regions, AE conditions, and resonance energies regardless of the presence of EMIC waves. EMIC waves occur when the anisotropy lies below but close to this upper bound within a narrow plasma β range: The lower cutoff β is due to an excessively high anisotropy threshold and the upper cutoff β is possibly due to the predominant role of a faster-growing mirror mode instability. We also find that the anisotropy during the observed EMIC waves is unstable, leading to the linear ion cyclotron instability. This result implies that the upper bound of the anisotropy is due to nonlinear processes.

1. Introduction

The anisotropic velocity distributions of charged particles have long been known to play an important roles in the excitation of cyclotron waves in space plasmas (e.g., Kennel and Petschek, 1966; Gary et al., 1976, 1994a,b, 2012; Kozyra et al., 1984; Hu et al., 1990; Denton et al., 1993, 1994; Chen et al., 2011; Silin et al., 2011; Lee et al., 2017). A parameter that quantifies the anisotropy of phase space density in velocity space is usually used to describe anisotropy-driven instability. The most popular choice is to use a simple definition given by the ratio between the parallel and perpendicular temperatures of the particles, ($A = \frac{T_\perp}{T_\parallel} - 1$), which is valid in the case of the bi-Maxwellian distribution function. A more general definition that can be applied to any distribution function was given by Kennel and Petschek (1966). This definition is used in the present work (see Section 2 below).

According to the linear perturbation theory, when the proton anisotropy is sufficiently increased to reach above a certain threshold condition by external sources, such as substorm injections or solar wind dynamic pressure enhancements (Cho et al., 2017), the particle state becomes unstable, leading to ion cyclotron instability thereby generating EMIC waves. EMIC waves have generally been accepted to play a critical role in outer radiation belt dynamics by scattering relativistic electrons. Previous studies have reported a rather low occurrence rate of EMIC waves in the Earth's inner magnetosphere ($L < 6$) during the Van Allen Probes mission era (Saikin et al., 2015; Wang et al., 2015; Noh et al., 2018). However, there has been a substantial accumulation of both theoretical and observational support for the EMIC wave-driven precipitation of relativistic electrons (e.g., Qin et al., 2020, and references therein).

Precise information detailing the observational characteristics of the proton distribution in velocity space is important to understand the EMIC wave excitation mechanism. Several studies have recently been carried out investigating proton distributions in the inner magnetosphere. Yue et al. (2017) investigated the characteristics of the pitch angle distributions of protons with energies of 1 eV to 600 keV near the equator. They demonstrate that the pitch angle distribution of the protons differs over different energy ranges. Plasmaspheric (several eV) and ring current (5 – 100 keV) protons usually have

a pancake distribution (flux peak at 90˚ of pitch angle). However, the warm plasma cloak (10 eV – several keV) shows a bi-directional distribution (flux peak at both 0˚ and 180˚) and the high energy protons (100 – 400 keV) show a butterfly distribution. They also reported that the pitch angle distribution can differ under various geomagnetic conditions. Artemyev et al. (2018) investigated the radial profile of the proton temperature anisotropy in the nightside equator region. They reported that the proton temperature anisotropy is higher at a low radial distance ($L < 6$) than high radial distance ($L > 6$). They also found that the overall proton temperature anisotropy decreases under enhanced geomagnetic activity, which is in turn energy-dependent. Imajo et al. (2019) investigated the proton temperature anisotropy in a meridional plane on the nightside during moderate storms. They found that the proton temperature anisotropy decreases statistically with radial distance, but the latitudinal dependence was not clear.

Plasma instabilities are often expressed in terms of the relationship between the particle anisotropy in velocity space and plasma beta (the ratio between the plasma pressure and magnetic pressure). There have been several studies that demonstrate the marginal stability conditions for the ion cyclotron instability in the solar wind and the magnetosphere can be expressed as an inverse relationship between the proton temperature anisotropy and the parallel proton beta ($\beta_{\parallel,p} = \frac{nk_B T_{\parallel,p}}{\frac{B^2}{2\mu_0}}$) (Gary et al., 1976, 1994a,b; Anderson et al., 1994; Gary and Lee 1994; Phan et al., 1994; Blum et al., 2009, 2012; Yue et al., 2019). According to the theory, if the plasma state exceeds the threshold anisotropy for a plasma beta that is given by the inverse relationship or vice versa, such plasma states can become unstable and the wave is amplified as it consumes free energy, relaxing the plasma state to a lower free energy state. However, in reality, the marginal stability conditions for trapped particles are complicated by various plasma parameters and the presence of heavy ions (Anderson et al., 1994; Phan et al., 1994; Lee et al., 2017; Noh et al., 2018). Thus, it is not easy to specify the limit for marginal stability with the sole use of a simple expression describing the inverse relationship in real-space plasmas.

In this study, we quantitatively determine the proton anisotropy parameter defined by Kennel and Petschek (1966) using long-term (from January 2013 to February 2018) measurements collected by the

98 Van Allen Probes in the inner magnetosphere. Our primary goal is to examine the inverse relationship
99 between the proton anisotropy parameter and the parallel proton beta $\beta_{\parallel,p}$ under various conditions (e.g.
100 MLT, MLAT, and geomagnetic conditions), regardless of EMIC wave occurrence. Ultimately, we aim
101 to demonstrate the implications of the inverse relationship with regard to ion cyclotron instability.
102

2. Data and methodology

The Van Allen Probe mission consists of two identical satellites (*Mauk et al.,* 2013) which were launched in August 2012 and completed their mission in October 2019. The orbit of the satellites covered a radial distance from 500 km to 30,600 km at an orbital inclination of ±10˚ which corresponds to approximately ±20˚ in magnetic latitude. The line of the apsides precessed longitudinally approximately 210˚/year. The data from Van Allen Probe-A is used in this study.

In order to calculate the anisotropy parameter, we use two particle detectors to cover a wide energy range. The Helium Oxygen Proton Electron plasma spectrometer (HOPE) covers the particle energy from 1 eV to - 52 keV and distinguishes H+, He+, and O+ (*Funsten et al.*, 2013). The Radiation Belt Storm Probes Ion Composition Experiment (RBSPICE) covers the energy range from 30 keV to 600 keV and also distinguishes heavy ions (He+ and O+) using time-of-flight technology (*Mitchell et al.*, 2013). Both instruments provide a pitch angle resolution covering the range of 0˚ to 180˚. The quality of the data gathered using HOPE (release 04) has recently been improved by inter-calibration with RBSPICE. The discrepancy between the high energy channel of HOPE and low energy channel of RBSPICE has thus been reduced to within a factor of 2 for 94% out of entire data.

The Electric and Magnetic Field Instrument Suite and Integrated Science (EMFISIS) measures the DC magnetic field in three orthogonal directions (*Kletzing et al.*, 2013). The sampling cadence is 64 Hz. In this study, the magnetic field intensity is used for calculating the proton beta and the 64 Hz vector magnetic field measurements to extract EMIC waves.

As noted in Section 1, we use the definition of the anisotropy parameter defined by Kennel and Petschek (1966):

$$\mathrm{A} = \frac{\int_0^\infty v_\perp \left(v_\parallel \frac{\partial f}{\partial v_\perp} - v_\perp \frac{\partial f}{\partial v_\parallel} \right) \frac{v_\perp}{v_\parallel} \, dv_\perp \Big|_{v_\parallel = v_r}}{2 \int_0^\infty v_\perp f \, dv_\perp \Big|_{v_\parallel = v_r}} \quad (1)$$

where $v_\perp, v_\parallel$ are the particle velocity components that are perpendicular and parallel to the background magnetic field, respectively. f is the distribution function of the particles and v_r is the

127 resonant velocity of the interacting particles. We use the same calculation method and criteria as those
128 in Noh et al. (2018). We concatenate HOPE (50eV – 52 keV) and RBSPICE (52 – 488 keV) in the order
129 of energy. Since HOPE has a sampling cadence of 22 seconds whereas that of RBSPICE is
130 approximately 10 seconds, we interpolate the RBSPICE sampling time to the HOPE sampling time.
131 The anisotropy parameters are calculated every minute. More details concerning the numerical
132 estimation of the anisotropy parameter are given in Noh et al. (2018).

133

3. Spatial distribution of anisotropy parameters

The spatial distributions of the calculated anisotropy parameters are examined. We distinguish the spatial distributions according to the level of the AE index. The AE index is used to ascertain the supply of energetic particles via substorms and enhanced convection from the plasma sheet into the inner magnetosphere. AE indices are sampled at the same time as the anisotropy parameter.

Figure 1(a) and 1(b) show the results for two selected energies. We emphasize that these were obtained without considering the existence of EMIC waves. Figure 1(a) shows the equatorial distribution of the anisotropy parameter at $E_{||}$ = 10 keV ($E_{\|} = \frac{1}{2} m_P v_{\|}$). The anisotropy parameter is higher in the lower L region, which is roughly the case for all AE conditions. Overall, while the anisotropy parameter slightly decreases as the AE increases, its radial gradient is steeper with increasing AE. In particular, the anisotropy parameter at higher L on the nightside is dramatically reduced as the AE increases. Consequently, the anisotropy parameter distribution becomes more asymmetric between dayside and nightside at higher L. This asymmetry is not significant in the lower L region (L < 4). Figure 1(b) shows the distributions of the anisotropy parameter at $E_{||}$ = 50 keV. While the main features are similar to the 10 keV case, the anisotropy is quantitatively somewhat lower than the case of 10 keV. This means that the energy dependence of the anisotropy is not reflected by a bi-Maxwellian distribution.

The spatial distributions detailing the comparison of the anisotropy with the parallel proton beta $\beta_{\|,p}$ are shown in Figure 1(c). The $\beta_{\|,p}$ increases on the duskside to the nightside at higher values of L and under higher AE index conditions. Importantly, based on visual inspection, there is an overall trend for an inverse relationship between the anisotropy parameter and the $\beta_{P,\|}$ at both energies. A detailed discussion of the feature of this is given in Section 4.

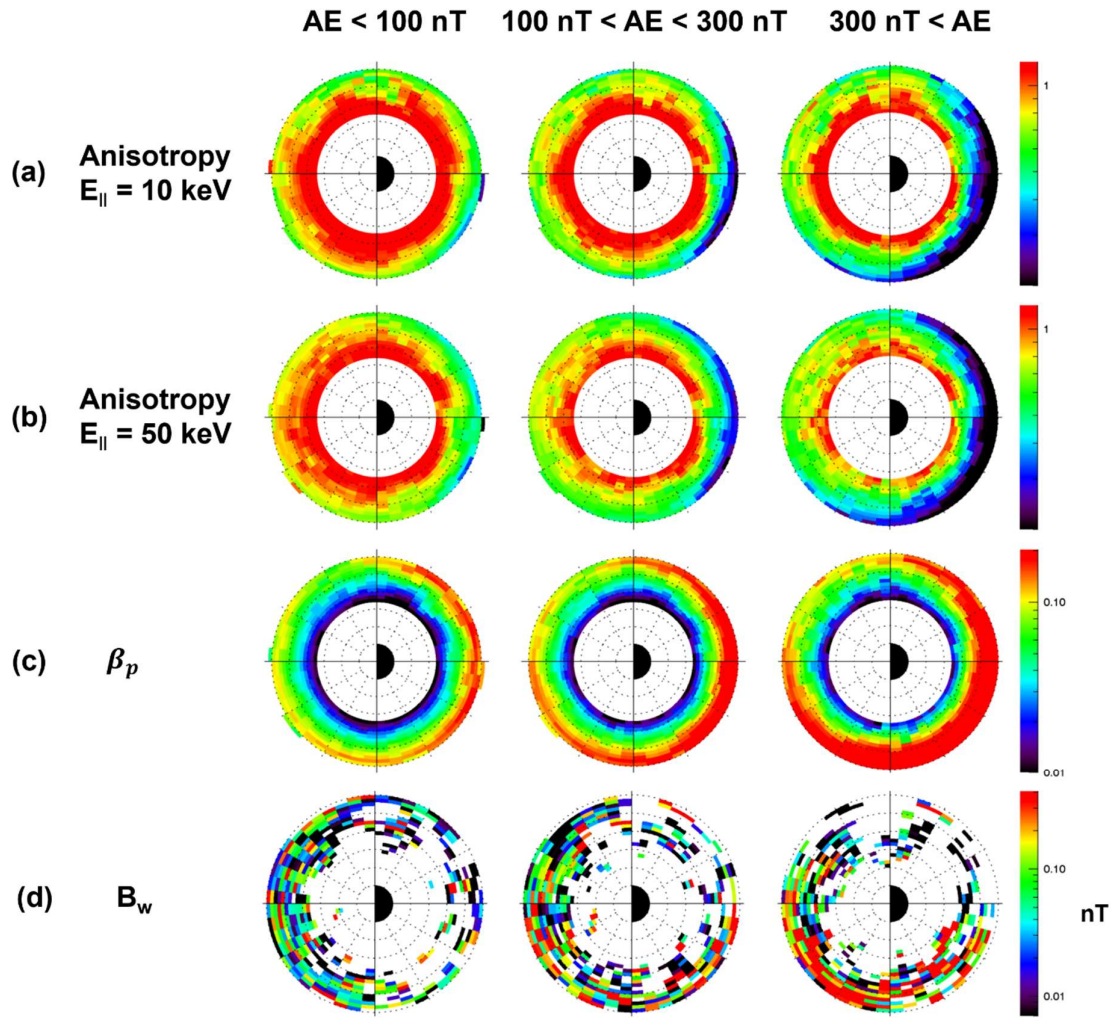

156

157 **Figure 1 L-MLT plane distribution of (a) Kennel-Petschek anisotropy at E = 10 keV, (b) the**
158 **anisotropy at E = 50 keV, (c) the parallel proton beta and (d) the amplitude of the EMIC waves**
159 **for three AE levels using the Van Allen Probes observations from January 2013 to February 2018.**
160 **All colors in each panel indicate the averaged parameters in each L and MLT bin. The dotted**
161 **circles refer to L= 2 to 6. The radially dotted lines indicate MLT ticks at 2 h intervals.**

162

The ultimate aim of this study is to examine the implications of the proton anisotropies and $\beta_{\parallel,p}$ on the EMIC wave excitation, on which we present details in the subsequent sections. For this purpose, we identified EMIC waves using the same wave detection algorithm as that used in Noh et al. (2018). Using this algorithm, 779 EMIC wave events were identified during the same interval used for the anisotropy and $\beta_{\parallel,p}$ statistics (January 2013 to February 2018). Figure 1(d) shows the spatial distribution of the amplitudes of the identified EMIC waves (B_w). The distributions cover nearly all MLTs and largely at $L > 3$. The wave amplitude increases in the high L afternoon region as the AE increases. By comparing this with the anisotropy and $\beta_{P,\parallel}$ in panels 1(a) to 1(c), we find a rough trend suggesting that this region corresponds to the overlapping region of high $\beta_{P,\parallel}$ and moderate anisotropy parameters. We additionally find that the occurrence rate of EMIC waves (not shown) increases under enhanced geomagnetic conditions (higher AE index) and is focused on the overlapping region where high $\beta_{P,\parallel}$ and anisotropy occur in a similar manner as the wave amplitudes.

4. Upper limits of anisotropy and corresponding $\beta_{\parallel,p}$ ranges

In this section, we examine the detailed aspects of the inverse relationship between the anisotropy parameter A and $\beta_{\parallel,p}$ revealed in Figure 1. Noh et al. (2018) suggested that the ion cyclotron instability threshold condition of Kennel and Petschek (1966) can be expressed via the inverse relation,

$$A = -\frac{1}{\varsigma_p^-}\left(\frac{\omega}{kv_A}\right)\left(\frac{1}{\sqrt{\beta_{\parallel,p}}}\right). \quad (2)$$

where A is the anisotropy parameter, $\varsigma_p^- = \frac{\omega-\Omega_p}{\sqrt{2}kv_{th}}$, $v_{th} = \sqrt{\frac{T_{\parallel,p}}{m_p}}$, k is the wave number and v_A is the Alfven speed.

We can further simplify this by incorporating the potential dependence of ς_p^- and $\frac{\omega}{kv_A}$ on $\beta_{\parallel,p}$ into the fitting parameters S and α,

$$A = \frac{S}{\beta_{\parallel,p}^{\alpha}}. \quad (3)$$

This formula is equivalent to the instability criterion suggested by Gary and Lee (1994) except that they specifically determined the dependence of ς_p^- and $\frac{\omega}{kv_A}$ on $\beta_{\parallel,p}$ by numerically solving the dispersion relation with a fixed growth and for a bi-Maxwellian distribution that is applicable to the Earth's magnetosheath.

The intent to determine the extent of the overall inverse relation shown in Figure 1 is consistent with the theoretically predicted inverse relation (3). We investigate the anisotropy parameter and $\beta_{\parallel,p}$ data in Figure 1 under various conditions by distinguishing the resonance energy $E_{\parallel}$ of the anisotropy parameter, MLT sector, MLAT, and AE index conditions. We divide the MLT into four sectors representing midnight (21 h – 03 h), dawn (03 h – 09 h), noon (09 h – 15 h) and dusk (15 h – 21 h). The MLAT is separated into two sections; that is, near-the-equator (|MLAT| ≤ 10˚) and off-the-equator (|MLAT| > 10˚). Three ranges are used for the AE index, as discussed in Section 3.

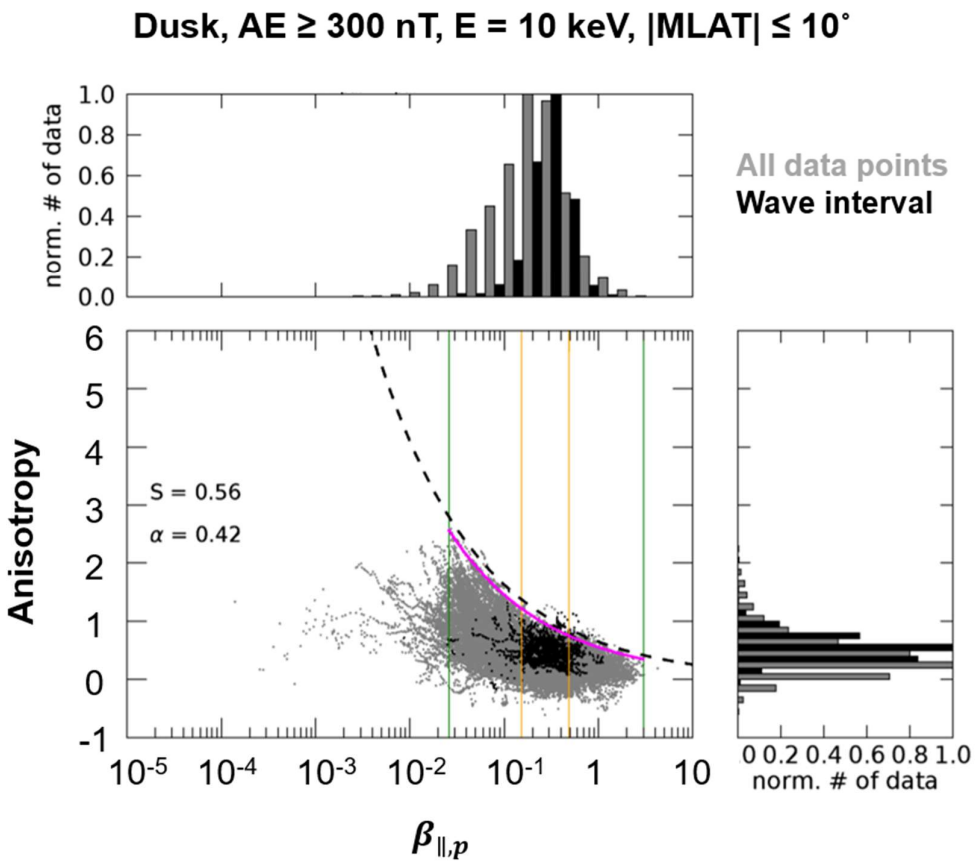

197

198 **Figure 2 Scatter plot of the anisotropy parameter at $E_{\parallel}$ = 10 keV and $\beta_{\parallel,p}$ under disturbed**
199 **conditions (AE index ≥ 300) on the dusk side near the equator. The gray and black dots in the**
200 **middle panel indicate all data points and those during EMIC wave intervals, respectively. The**
201 **solid magenta is the fit curve of the upper bound of the anisotropy parameter in the finite $\beta_{\parallel,p}$**
202 **range. The $\beta_{\parallel,p}$ range of upper bound is denoted by green vertical lines. The black dashed line is**
203 **the inverse relation of the anisotropy and $\beta_{\parallel,p}$ as suggested by Gary et al. (1994a). The orange**
204 **vertical lines are the bottom and top 10 percent of the $\beta_{\parallel,p}$ in which EMIC waves are observed.**
205 **The upper panel is a histogram of the $\beta_{\parallel,p}$ values in the study, and the right panel is a histogram**
206 **of the anisotropy parameters.**

207

208 Figure 2 is a scatter plot of the anisotropy parameter at $E_{\parallel}$ = 10 keV and the $\beta_{\parallel,p}$ taken from Figures

1(a) and 1(c) and meet the conditions, 15 h ≤ MLT < 21 h, |MLAT| ≤ 10°, AE > 300 nT. While the gray dots refer to all the data points from Figure 1(a) and 1(c) under this set of conditions, the black dots are the cases in which the EMIC waves are observed. Several interesting features can be identified from Figure 2. The most prominent feature is that there is a clear upper bound to the anisotropy parameter, which is inversely proportional to $\beta_{\parallel,p}$. This upper bound of the anisotropy parameter is well represented by the inverse relationship formula in Eq. (3), with S = 0.56 and $\alpha = 0.42$ (magenta curve). The range of $\beta_{\parallel,p}$ that this upper bound follows the inverse relationship is confined within a certain $\beta_{\parallel,p}$ range from 2.7×10^{-2} to 3.0 (vertical green lines) rather than the entire $\beta_{\parallel,p}$ range that was measured. For reference, the threshold curve suggested by Gary et al. (1994a) is added, with the growth rate of 10^{-2} times the wave's real frequency (black dashed line), which corresponds to S = 0.65 and $\alpha = 0.4$ in Eq. (3). Gary et al's curve is similar to the upper bound curve generated in this study. This leads to the question of whether these observations imply stable conditions for the development of ion cyclotron instability predicted by the inverse relation. We will discuss this in the next section.

Second, EMIC waves (black dots) are observed in a $\beta_{\parallel,p}$ range that is narrower than that of the upper bound curve: approximately 80% of the EMIC wave events detected lie between $\beta_{\parallel,p} = 1.7\times10^{-1}$ and 5.0×10^{-1} (vertical orange lines). Beyond this range, the occurrence of EMIC waves becomes rare. This trend at higher $\beta_{\parallel,p}$ is particularly interesting because one might expect a higher possibility of EMIC wave occurrence for higher beta due to the lower anisotropy threshold. The result here implies that a high beta alone does not necessarily guarantee the occurrence of ion cyclotron instability, but rather an additional mechanism needs to be identified. We discuss this further in Section 6. Lastly, the anisotropy parameter during the EMIC wave intervals lies in high value ranges mostly close enough to the upper bound curve. To further address this feature, an instability test is performed and is discussed in the subsequent section.

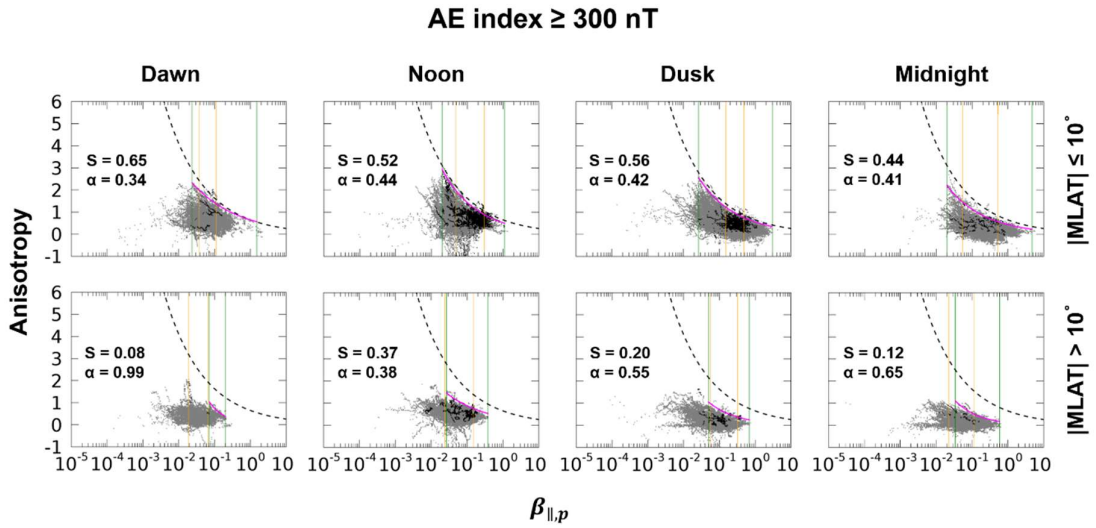

Figure 3 Scatter plots for the anisotropy at $E_{||}$ = 10 keV and $\beta_{\parallel,p}$ which are sorted by MLT sector and MLAT (AE index ≥ 300 nT). The top third panel from the left is same as that in Figure 3. Each panel has the same format as Figure 3.

In Figures 3 to 5, we examine whether the three main features found above are also observed in other spatial regions and for different AE conditions and parallel energies. Figure 3 shows the results of the spatial dependence for four different MLT sectors and two MLAT regions. The third panel in the first row is the same as that in Figure 2.

Figure 3 reveals several interesting features. First, we find that a well-defined upper bound of the anisotropy is present in the form of an inverse relation in all the MLT and MLAT zones. We note that the beta range for the upper bound curves (green vertical lines) differs in different spatial zones. However, this is primarily due to the configuration of the magnetic field, where high beta measurements are preferentially observed in low magnetic field regions such as near midnight and near the equator. We also point out that the fitting coefficient S values are lower in the higher latitude zone than near the equator, indicating that the anisotropy is overall lower in the higher latitude zone. It is interesting that the upper bound curve (magenta line) lies well below the threshold curve (black dashed line) given by Gary et al. (1994a). Second, the EMIC waves (black dots) are observed most frequently in the noon and dusk sectors near the equator; only a limited percentage of the wave events are observed in the dawn

sector, both near and off the equator. The anisotropy values of these events are mostly close to the upper bound curves. In addition, when they are present, the occurrence of EMIC waves is limited to a specific range of $\beta_{\parallel,p}$ (orange lines) for all MLT and MLAT zones and the absence of EMIC wave occurrence in the higher beta range is a common feature in all the spatial zones. In short, although the details are somewhat different, there are three main features common to most MLT and MLAT zones: (i) a well-defined upper bound to the anisotropy in the form of an inverse relation, (ii) a limited beta range for EMIC waves with an upper cutoff beta value, and (iii) the proximity of the EMIC wave anisotropy to the upper bounds.

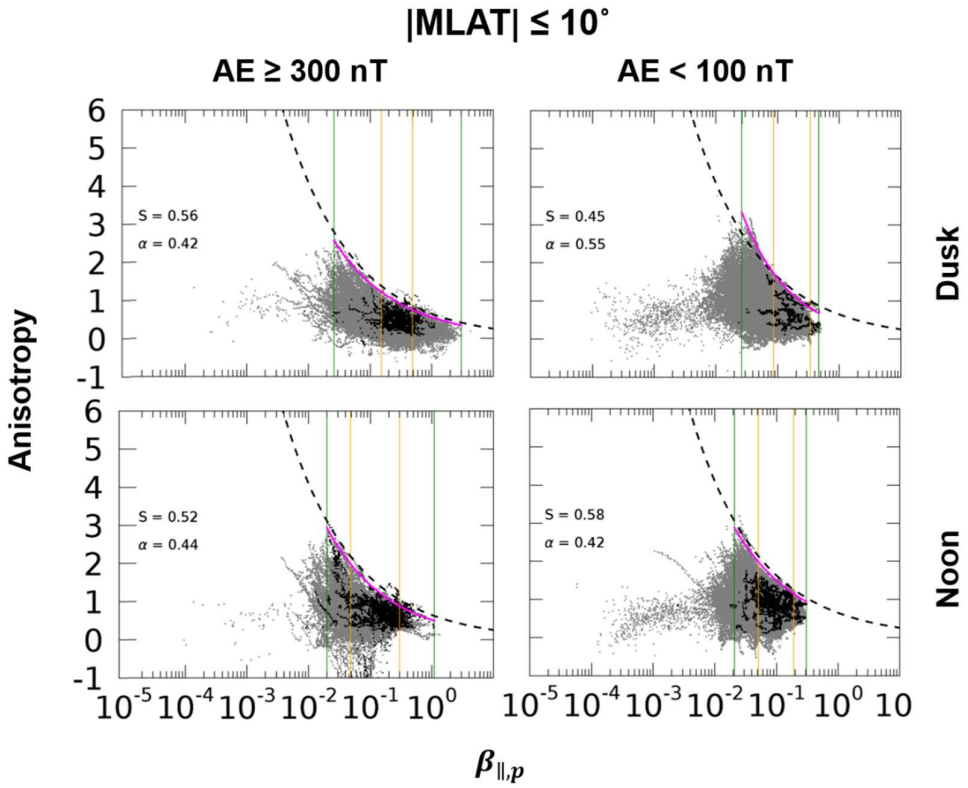

Figure 4 Scatter plots for the anisotropy at $E_{\parallel}$ = 10 keV and $\beta_{\parallel,p}$ for AE ≥ 300 (left column) and AE < 100 (right column) in the dusk (upper row) and noon (bottom row) sectors. All data are from the near-equator (|MLAT| ≤ 10°).

Figure 4 examines the dependence on the AE index of the near-equatorial region on the noon and duskside. Attention is particularly paid to the MLT and MLAT zones where the EMIC waves are

most frequent. While the $\beta_{\parallel,p}$ ranges are narrower under low AE conditions over the entire data set, the $\beta_{\parallel,p}$ ranges of the EMIC waves are similar at both high and low AE conditions. Consequently, for low AE conditions, the upper cutoff of $\beta_{\parallel,p}$ for the EMIC waves almost coincides with the $\beta_{\parallel,p}$ ranges for the upper bound, whereas the upper cutoff of $\beta_{\parallel,p}$ for the EMIC wave is below that of the upper bound for the high AE. This result implies that an increase in the AE activity leads to high beta states in which the EMIC waves are not necessarily triggered while the inverse relationship between the anisotropy and plasma beta continues to hold.

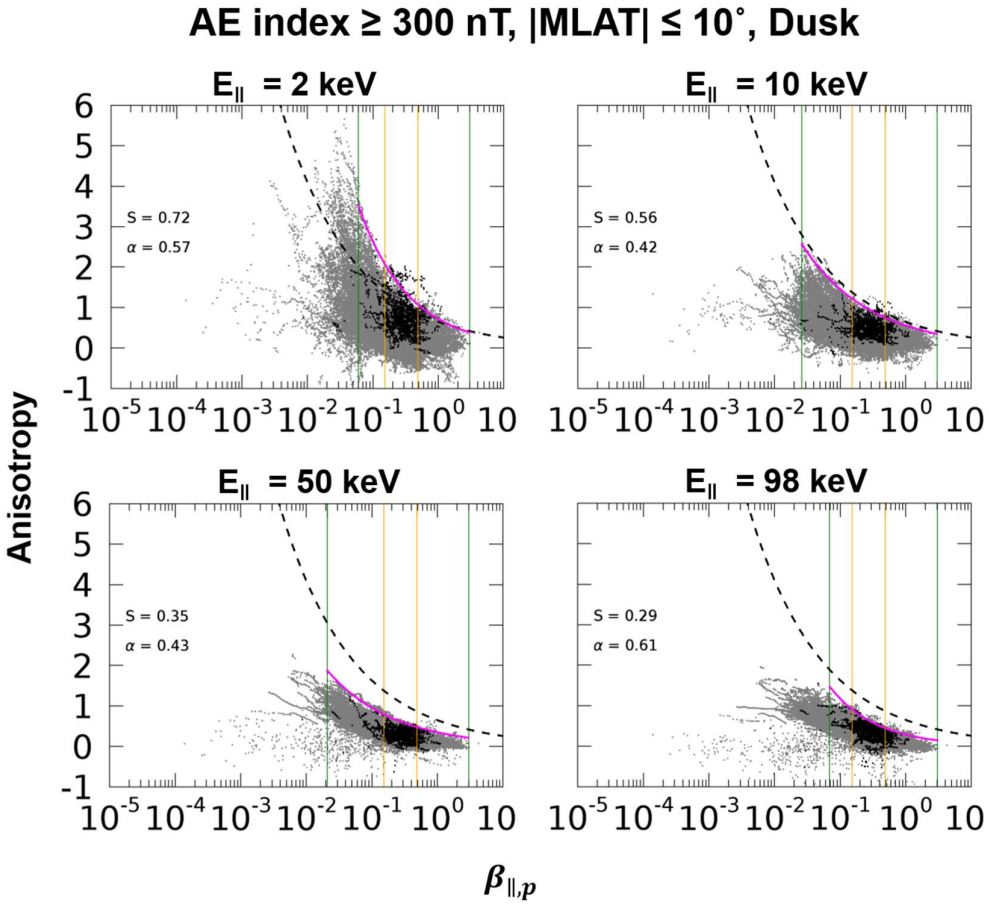

Figure 5 Scatter plots of the anisotropy parameter at $E_{\parallel}$ = 2, 10, 50 and 98 keV and $\beta_{\parallel,p}$ for the same MLT and MLAT sector with the same AE index ≥ 300 nT. Top right panel is same as Figure 2. Each panel has the same format as Figure 2.

As noted in the Introduction, unless the distribution function of the proton is single bi-Maxwellian distribution, the anisotropy parameter can differ by its parallel energy. We calculate the anisotropy

parameters for a range of parallel energies that are considered suitable for the development of ion cyclotron resonance instability. Figure 5 shows the relationship between the anisotropy parameter and $\beta_{\parallel,p}$ for parallel energies of 2, 10, 50, and 98 keV under the same conditions as those in Figure 2 (AE index $\geq$ 300 nT, dusk sector, and |MLAT| $\leq$ 10 ˚). The 10 keV result in Figure 2 is repeated here for comparison (upper right panel). Overall, the three main features identified for the 10 keV case in Figure 2 are also observed for the other energies in Figure 5.

One difference that is observed at different energies is that while the anisotropy parameters have a clear upper bound that follows the inverse relation under all the energies, the anisotropies are higher overall at lower energies and their upper bound curves are steeper for lower energies as well (compare the coefficients S and α among the four energies). Note that the beta ranges are the same for all the energies as the chosen parallel energy enters the calculation of the anisotropy parameter without affecting the plasma beta. One further interesting feature is that the anisotropy at $E_{\parallel}$ = 98 keV still shows an upper bound, but it is less clear than that at lower energies and the beta range of the upper bound is narrower. While the proton populations at $E_{\parallel}$ = 98 keV lie within the typical resonant energy range, the most effective energy range for the ion cyclotron instability is approximately a few tens of keV (Meredith et al. 2003). Thus, particles at $E_{\parallel}$ = 98 keV can be less affected by the ion cyclotron instability than those at lower energy. Another point to note is that the curve produced by Gary et al. (1994a) is fixed in a manner independent of the specific energies, as the anisotropy parameter is based on single bi-Maxwellian distribution. The upper bound at 10 keV almost coincides with the curve from Gary et al., whereas the upper bound curves for the other parallel energies differ from the prediction in Gary et al. In short, while the three main features in Figure 2 are present at all energies, the specific anisotropy values and their inverse relations with $\beta_{\parallel,p}$ are dependent on the resonant parallel energies, which is unlike the simple inverse relation such as that of Gary et al. (1994a).

5. Linear instability test

In Section 4, we found that there is generally a well-defined upper bound for the anisotropy parameter in the form of an inverse relation with the plasma beta over a broad range of spatial locations and AE conditions. When they occur, EMIC waves are associated with an anisotropy below (but mostly close to) this upper bound. A question naturally arises regarding the stability of the observed anisotropic protons. What determines the upper bound of the anisotropy in an inverse-relation way? Are the EMIC waves with the observed proton anisotropies a manifestation of a stable state, an ongoing instability, or a saturated state of an already grown instability? This section examines some of these questions by testing the linear instability criterion for the development of an ion cyclotron instability with the observed anisotropy parameter. Specifically, we utilize the discriminant for ion cyclotron instability taken from eq. (2.23) in Kennel and Petschek (1966):

$$A\left(\frac{\Omega_P}{\omega} - 1\right) > 1. \quad (4)$$

As the discriminant requires the wave frequency, we can test this only when EMIC wave events occur. Note that this criterion cannot be used to estimate the local growth rate and can only determine whether the growth rate of the wave will be positive or negative (growing or damping). Note that the discriminant is obtained from the assumption of an electron-proton plasma; thus, any effects caused by the presence of heavier ions could be missing.

Figure 6 shows the estimation results of the left-hand side of Eq. (4) for the EMIC wave events in Figure 1 using anisotropy parameters for parallel energies from 6 to 98 keV. The estimations are determined during each EMIC wave interval and the resulting time-series curves are superposed. The results in Figure 6 are distinguished by location, as discussed in Section 4. The horizontal gray line in each panel indicates the linear instability threshold. Although the discriminant differs by location and parallel energy, the superposed discriminants are all well above the threshold value. This means that EMIC waves with the measured anisotropy parameters, which are all below the upper bound, are still in a linearly unstable state. This implies that the upper bound of the anisotropy (at least above the EMIC

wave beta range) is not set by the linear instability but rather requires an additional process such as a nonlinear development. The satisfaction of the linear instability implies a continuous supply of free energy in the form of a still anisotropic distribution to complement its consumption to drive the wave growth.

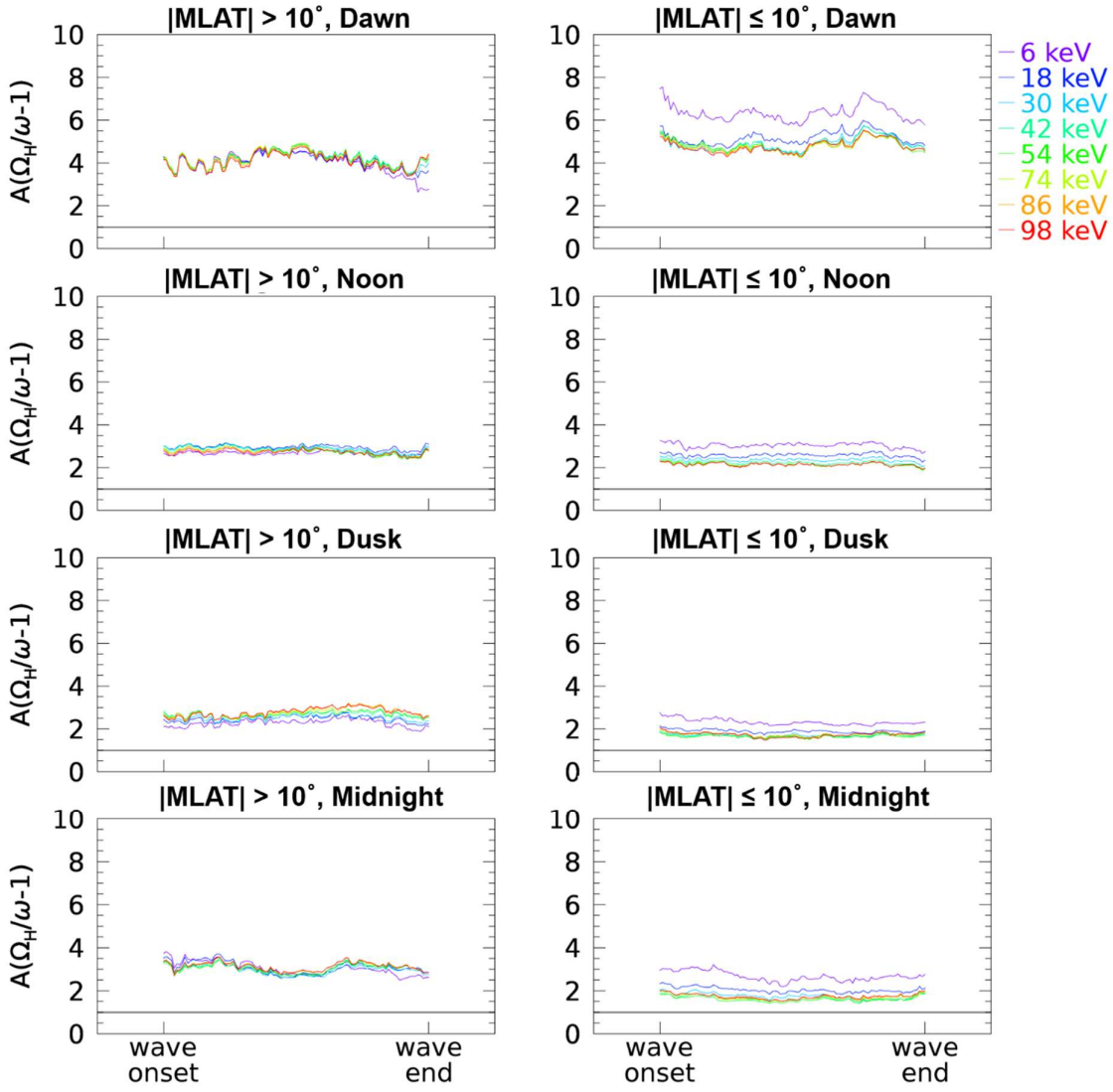

Figure 6 Superposed epoch analysis of the wave events for both high MLAT (|MLAT| > 10˚, left column) and low MLAT (|MLAT| < 10˚, right column). The MLT sectors are defined in the same manner as discussed in Section 4. The lines are distinguished by color which indicates the parallel energy of the anisotropy parameter. Gray lines in each panel are the linear instability threshold.

6. Summary and discussion

In this study, we examined the anisotropy parameter defined by Kennel & Petschek (1966) with resonant parallel energy from 1 keV to 100 keV and $\beta_{\parallel,p}$ using Van Allen Probe measurements. We found an overall trend in that the anisotropy parameters and $\beta_{\parallel,p}$ are inversely related to each other over a wide range of spatial regions and AE conditions, regardless of the occurrence of EMIC waves. The main results that we found are as follows,

i) The anisotropy is limited by a clear upper bound that varies inversely with $\beta_{\parallel,p}$ over a wide range of locations, AE index conditions, and resonant parallel energies, regardless of the existence of EMIC waves.

ii) The clear upper bound of the anisotropy parameter exists within a certain $\beta_{\parallel,p}$ range (~10^{-2} – a few) and varies slightly with respect to location and AE index condition.

iii) EMIC waves are mostly observed over a limited $\beta_{\parallel,p}$ range with lower and upper cutoff values (approximately 10^{-1} to < 1).

iv) EMIC waves are found with anisotropies below, but mostly close to, the upper bound. This anisotropy satisfies the linear instability criterion for the ion cyclotron mode.

Noh et al. (2018) demonstrated that the linear threshold conditions can differ significantly in terms of the inverse relationship between the anisotropy and $\beta_{\parallel,p}$ depending on the specific plasma conditions. It is reasonable to expect that each observed wave event has its own threshold condition according to the plasma conditions, which can vary to a large extent from event to event. Despite this possible diversity, the main result (i) of this study suggests the existence of a clear upper bound for the anisotropy parameter above which nature does not allow. We suggest calling each upper bound of the anisotropy parameter the “regional stability condition”.

The absence of EMIC waves below the lower cutoff beta value (result (iii) above) is expected as a low $\beta_{\parallel,p}$ would require a very high anisotropy threshold for ion cyclotron instability, which is hardly

realized. Consequently, a large anisotropy can occur without EMIC wave amplification in low beta conditions; for example, the anisotropy at $E_{||}$ = 10 keV near the equator on the duskside can reach 2 or more (see Figure 2). We suggest that the usual anisotropy drivers, such as substorm particle injection and dayside compression can hardly provide large enough anisotropies in the inner magnetosphere where the $\beta_{||,p}$ is too low.

The absence of EMIC waves above the upper cutoff beta value (result (iii) above) implies that some type of instability other than ion cyclotron instability must play a role in setting the upper bound of the anisotropy. For the high $\beta_{||,p}$ region, mirror mode instability may operate more efficiently than ion cyclotron instability and can consume free energy faster so that EMIC waves do not grow sufficiently (Anderson and Fuselier, 1993; Gary et al., 1993; Lacombe and Belmont, 1995; Shoji et al., 2009; Yoon and Seough, 2012). Both mirror mode and ion cyclotron instabilities are excited by the anisotropic distribution of the protons. It has been reported that ion cyclotron instability is more dominant in lower $\beta_{||,p}$ conditions whereas higher $\beta_{||,p}$ conditions are favorable for mirror instabilities. Gary et al. (1993) used the linear theory to demonstrate that the inverse relationship between anisotropy and $\beta_{||,p}$ for both ion cyclotron instability and mirror mode instability crosses near $\beta_{||,p}$ of approximately 1. Thus the threshold anisotropy for the mirror mode instability is lower than that of ion cyclotron instability in a high $\beta_{||,p}$ regime. Yoon and Seough (2012) have demonstrated similar results using the quasi-linear theory that the mirror mode wave dominates the EMIC wave near the saturation stage of the waves. Shoji et al. (2009) conducted a 3D particle-in-cell simulation of anisotropic plasmas in which they found that the mirror mode instability efficiently relaxes the anisotropy so that the growth rate of the ion cyclotron instability becomes weaker before saturation.

Our result (iv) implies the possibility that an additional process accompanies the linear instability to produce the observed anisotropies during the EMIC waves. Recently, Yue et al. (2019) reported an inverse relationship between temperature anisotropy and $\beta_{||,p}$. They assumed that the observed proton distributions are already in a stable state to the linear ion cyclotron mode, unlike the findings in this study. We suggest that the upper bound of the anisotropy is possibly caused by a nonlinear saturation

process (Gary et al., 1993; Bortnik et al., 2011; Silin et al., 2011; Min et al., 2015; Ofman et al., 2017). Although the observed EMIC waves are linearly unstable, the clear presence of the upper bound of the anisotropy parameter implies that there must be a saturation process for proton anisotropy in a nonlinear stage. After the linear growth stage, amplified waves feedback to the source protons, then the distribution of the protons modifies the growth rate. This self-consistent process results in the saturation stage of both waves and particle distribution.

Lastly, the linear instability criterion used in Section 5 does not include the presence of heavy ions. Helium ions can raise the threshold conditions for ion cyclotron instability (Matteini et al., 2012). The contribution of hot He+ ions to the growth rate can depend on the relative population of hot protons (Lee et al., 2017; Noh et al., 2018). Consideration of these hot heavy ions is therefore necessary to the extent at which it affects the inverse relation. This will be addressed in work in progress.

Acknowledgments

The work at the New Jersey Institute of Technology (NJIT) was supported by NSF under grant AGS-1602560 and the NASA Van Allen Probes RBSPICE instrument project, as supported by JHU/APL Subcontract No. 131803 to NJIT under NASA Prime Contract No. NNN06AA01C. The authors would like to thank the Van Allen Probes teams (EMFISIS, ECT, RBSPICE) for providing data utilized in this study. All Van Allen Probes data are publicly available on the following websites: http://www.RBSP-ect.lanl.gov/ (ECT); https://emfisis.physics.uiowa.edu/data/index (EMFISIS) and http://rbspice.ftecs.com/Data.html (RBSPICE).

References

Allen, R. C., J.-C. Zhang, L. M. Kistler, H. E. Spence, R.-L. Lin, B. Klecker, M. W. Dunlop, M. André, and V. K. Jordanova (2016), A statistical study of EMIC waves observed by Cluster: 2. Associated plasma conditions, *J. Geophys. Res. Space Physics*, 121, 6458–6479, doi:10.1002/2016JA022541.

Anderson, B. J. and S. A. Fuselier (1993), Magnetic Pulsations From 0.1 to 4.0 Hz and Associated Plasma Properties in the Earth's Subsolar Magnetosheath and Plasma Depletion Layer*, J. Geophys. Res., 98*, 1461-1479.

Anderson, B. J., S. A. Fuselier, S. P. Gary, and R. E. Denton (1994), Magnetic spectral signatures in the Earth's magnetosheath and plasma depletion layer*, J. Geophys. Res., 99*, 5877-5891.

Artemyev, A. V., X.-J. Zhang, V. Angelopoulos, A. Runov, H. E. Spence, & B. A. Larsen (2018). Plasma anisotropies and currents in the near-Earth plasma sheet and inner magnetosphere. *J. Geophys. Res. Space Physics: Space Physics*, 123, 5625–5639. https://doi.org/10.1029/2018JA025232

Blum, L. W., E. A. MacDonald, S. P. Gary, M. F. Thomsen, and H. E. Spence (2009), Ion observations from geosynchronous orbit as a proxy for ion cyclotron wave growth during storm times*, J. Geophys. Res., 114*, A10214, doi:10.1029/2009JA014396.

Blum, L. W., et al. (2012), A comparison of magnetic field measurements and a plasma-based proxy to infer EMIC wave distributions at geosynchronous orbit, *J. Geophys. Res.*, 117, A05220, doi:10.1029/2011JA017474.

Bortnik, J., N. Omidi, L. Chen, R. M. Thorne, and R. B. Horne (2011), Saturation characteristics of electromagnetic ion cyclotron waves, *J. Geophys. Res.,* 116, A09219, doi:10.1029/2011JA016638.

Chen, L., R. M. Thorne, and J. Bortnik (2011), The controlling effect of ion temperature on EMIC wave excitation and scattering, *Geophys. Res. Lett*., 38, L16109, doi:10.1029/2011GL048653.

Denton, R. E., M. K. Hudson, S. A. Fuselier, and B. J. Anderson (1993), Electromagnetic ion cyclotron waves in the plasma depletion layer, *J. Geophys. Res.*, 98, 13,477–13,490.

Denton, R. E., S. P. Gary, B. J. Anderson, S. A. Fuselier, and M. K. Hudson (1994), Low-frequency magnetic fluctuation spectra in the magnetosheath and plasma depletion layer, *J. Geophys. Res*., 99, 5893–5901, doi:10.1029/93JA02729.

Funsten, H., et al. (2013), Helium, oxygen, proton, and electron (HOPE) mass spectrometer for the radiation belt storm probes mission*, Space Sci. Rev.,* 179, 1-4, 423-484, doi:10.1007/s11214-013-9968-7

Gary, S. P. and M. A. Lee (1994), The ion cyclotron anisotropy instability and the inverse correlation between proton anisotropy and proton beta*, J. Geophys. Res.,* 99(A6), 11297-11301.

Gary, S. P., M. D. Montgomery, W. C. Feldman, and D. W. Forslund, (1976), Proton temperature anisotropy instabilities in the solar wind, *J. Geophys. Res.,* 81

Gary, S. P., M. E. McKean, D. Winske, B. J. Anderson, R. E. Denton, and S. A. Fuselier (1994a), The proton cyclotron instability and the anisotropy/beta inverse correlation, *J. Geophys. Res., 99*, 5903-5914.

Gary, S. P., M. B. Moldwin, M. F. Thomsen, D. Winske, and D. J. McComas (1994b), Hot proton anisotropies and cool proton temperatures in the outer magnetosphere, *J. Geophys. Res., 99*, 23603-23615.

Gary, S. P., K. Liu, and L. Chen (2012), Alfvén-cyclotron instability with singly ionized helium: Linear theory, *J. Geophys. Res*., 117, A08201, doi:10.1029/2012JA017740.

Gary, S., R. M. E. McKean, and D. Winske (1993), Ion cyclotron anisotropy instabilityes in the magnetosheath: Theory and simulations, *J. Geophys. Res. Space Physics,* 98, 3963-3971

Hu, Y. D., B. J. Fraser, and J.V. Olson (1990), Amplification of electromagnetic ion cyclotron waves along a wave path in the Earth's multicomponent magnetosphere, *Geophys. Res. Lett*., 17, 1053-1056.

Imajo, S., M. Nosé, S. Kasahara, S. Yokota, A. Matsuoka, K. Keika, et al. (2019), Meridional distribution of middle-energy protons and pressure-driven currents in the nightside inner magnetosphere: Arase observations, *J. Geophys. Res. Space Physics*, 124, 5719–5733. https://doi.org/10.1029/2019JA026682

480 Kennel, C. F., and H. E. Petschek, (1966), Limit on stably trapped particle fluxes, *J. Geophys. Res*.,
481 71(1), 1–28, doi:10.1029/JZ071i001p00001.

482

483 Kletzing, C. A., et. al., (2013), The Electric and Magnetic Field Instrument Suite and Integrated Science
484 (EMFISIS) on RBSP, *Space Sci. Rev*., 179, 1–4, doi:10.1007/S11214-013-9993-6.

485

486 Kozyra, J. U., T. E. Cravens, A.F. Nagy, and E. G. Fontheim (1984), Effects of energetic heavy ions on
487 electromagnetic ion cyclotron wave generation in the plasmapause region, *J. Geophys. Res*., 89, 2217-
488 2233.

489

490 Lacombe, C., and G. Belmont (1995), Waves in the Earth's magnetosheath: Observations and
491 interpretations, *Adv. Space Res.*, 15(8/9), 329

492

493 Lee, D. -Y., S. -J. Noh, C. -R. Choi, J. J. Lee, and J. A. Hwang (2017), Effect of hot anisotropic He+
494 ions on the growth and damping of electromagnetic ion cyclotron waves in the inner magnetosphere*, J.*
495 *Geophys. Res., 112*, 4935-4942, doi:10.1002/2016JA023826.

496

497 Lin, R. -L., et al. (2014), Testing linear theory of EMIC waves in the inner magnetosphere: Cluster
498 observations, *J. Geophys. Res. Space Physics*, 119, 1004–1027, doi:10.1002/2013JA019541.

499

500 Matteini, L., P. Hellinger, S. Landi, P. M. Travinicek, M. Velli (2012), Ion Kinetics in the Solar Wind:
501 Coupling Global Expansion to Local Microphysics, *Space Sci. Rev.*, 172, 373-396, DOI
502 10.1007/s11214-011-9774-z

Mauk, B. H., N. J. Fox, S. G. Kanekal, R. L. Kessel, D. G. Sibeck, and A. Ukhorskiy (2013), Science objectives and rationale for the Radiation Belt Storm Probes Mission, *Space Sci. Rev.*, doi:10.1007/s11214-012-9908-y.

Meredith, N. P., R. M. Thorne, R. B. Horne, D. Summers, B. J. Fraser, R. R. Anderson (2003), Statistical analysis of relativistic electron energies for cyclotron resonanace with EMIC waves observed on CRRES, *J. Geophys. Res*., 108(A6), 1250, doi:10.1029/2002JA009700.

Min, K., et al. (2015), Study of EMIC wave excitation using direct ion measurements, *J. Geophys. Res.*, 120, 2702–2719, doi:10.1002/2014JA020717.

Mitchell, D., et al. (2013), Radiation Belt Storm Probes Ion Composition Experiment (RBSPICE), *Space Sci. Rev.,* 179, 1-4, 263-308, doi: 10.1007/s11214-013-9965-x.

Noh, S.-J., D.-Y. Lee, C.-R. Choi, H. Kim, and R. Skoug (2018), Test of ion cyclotron resonance instability using proton distributions obtained from Van Allen Probe-A observations, *J. Geophys. Res. Space Physics*, 123. https://doi.org/10.1029/2018JA025385

Ofman, L., R. E. Denton, J. Bortnik, X. An, A. Glocer, and C. Komar (2017), Growth and nonlinear saturation of electromagnetic ion cyclotron waves in multi-ion species magnetospheric plasma, *J. Geophys. Res.*, 122, 6469–6484, doi:10.1002/2017JA024172.

526 Phan, T. -D., G. Pashmann, W. Baumjohann, and N. Sckopke (1994), The magnetosheath region
527 adjacent to the dayside magnetopause: AMPTE/IRM observations, *J. Geophys. Res., 99*, 121-141.

528

529 Qin, M., M. Hudson, R. Millan, L. Woodger, & X. Shen (2020). Statistical dependence of EMIC wave
530 scattering on wave and plasma parameters. *J. Geophys. Res. Space Physics*, 125, e2020JA027772.
531 https://doi.org/10. 1029/2020JA027772

532

533 Saikin, A. A., J.-C. Zhang, R. C. Allen, C. W. Smith, L. M. Kistler, H. E. Spence, R. B. Torbert, C. A.
534 Kletzing, and V. K. Jordanova (2015), The occurrence and wave properties of H+-, He+-, and O+-
535 band EMIC waves observed by the Van Allen Probes, *J. Geophys. Res. Space Physics*, 120,
536 doi:10.1002/2015JA021358.

537

538 Shoji, M., Y. Omura, B. T. Tsurutani, O. P. Verkhoglyadova, and B. Lembege (2009), Mirror instability
539 and L-mode electromagnetic ion cyclotron instability: Competition in the Earth's magnetosheath, *J.*
540 *Geophys. Res.*, 114, A10203, doi:10.1029/2008JA014038.

541

542 Silin, I., I. R. Mann, R. D. Sydora, D. Summers, and R. L. Mace (2011), Warm plasma effects on
543 electromagnetic ion cyclotron wave MeV electron interactions in the magnetosphere, *J. Geophys. Res*.,
544 116, A05215, doi:10.1029/2010JA016398.

545

546 Spasojevic, M., et al. (2011), Correspondence between a plasma-based EMIC wave proxy and
547 subauroral proton precipitation, *Geophys. Res. Lett*., 38, L23102, doi:10.1029/2011GL049735.

548

549 Summers, D., and R. M. Thorne (2003), Relativistic electron pitch-angle scattering by electromagnetic
550 ion cyclotron waves during geomagnetic storms, *J. Geophys. Res*., 108(A4), 1143,
551 doi:10.1029/2002JA009489.

552

553 Wang, D., et al. (2015), Statistical characteristics of EMIC waves: Van Allen Probe observations, *J.*
554 *Geophys. Res. Space Physics*, 120, 4400–4408, doi:10.1002/2015JA021089.

555

556 Yoon, P. H., and J. Seough (2012), Quasilinear theory of anisotropy-beta relation for combined mirror
557 and proton cyclotron instabilities, *J. Geophys. Res.,* 117, A08102, doi:10.1029/2012JA017697.

558

559 Yue, C., C.-W. Jun, J. Bortnik, X. An, Q. Ma, G. D. Reeves, et al. (2019), The relationship between
560 EMIC wave properties and proton distributions based on Van Allen probes observations, *Geophys. Res.*
561 *Lett*., 46. https://doi.org/10.1029/ 2019GL082633

562

563 Yue, C., J. Bortnik, R. M. Thorne, Q. Ma, X. An, C. R. Chappell, … C. A. Kletzing (2017), The
564 characteristic pitch angle distributions of 1 eV to 600 keV protons near the equator based on Van Allen
565 Probes observations, *J. Geophys. Res. Space Physics*, 122, 9464–9473. https://doi.org/10.1002/
566 2017JA024421